Precise Surface Profiling at the Nanoscale Enabled by Deep Learning

Lalith Krishna Samanth Bonagiri[1,2], Zirui Wang[3], Shan Zhou[1,3], and Yingjie Zhang[1,3,4]*

1. Materials Research Laboratory, University of Illinois, Urbana, Illinois 61801, USA

2. Department of Mechanical Science and Engineering, University of Illinois, Urbana, Illinois 61801, USA

3. Department of Materials Science and Engineering, University of Illinois, Urbana, Illinois 61801, USA

4. Beckman Institute for Advanced Science and Technology, University of Illinois, Urbana, Illinois 61801, USA

*Correspondence to: yjz@illinois.edu

Abstract: Surface topography, or height profile, is a critical property for various micro- and nano-structured materials, devices, as well as biological systems. At the nanoscale, atomic force microscopy (AFM) is the tool of choice for surface profiling, due to its capability to noninvasively map the topography of almost all types of samples. However, this method suffers from one drawback: the convolution of the nanoprobe's shape in the height profile of the samples, which is especially severe for sharp protrusion features. Here, we report a deep learning (DL) approach to overcome this limit. Adopting an image-to-image translation methodology, we use datasets of tip-convoluted and deconvoluted image pairs to train an encoder-decoder based deep convolutional neural network. The trained network successfully removes the tip convolution from AFM topographic images of various nano-corrugated surfaces and recovers the true, precise 3D height profiles of these samples.

Keywords: Surface profiling, atomic force microscopy, deep learning, machine learning, tip-convolution, nanoscale imaging.

Surface height profile is a key feature for monitoring and understanding the functions of various natural and engineered systems,[1] such as the processing and integration of nano-electronic devices,[2,3] the hydrophilicity/hydrophobicity of microstructured films/surfaces,[4,5] and the signal transduction of cell membranes.[6] The past few decades has seen significant progress in imaging technologies, as various optical,[7–10] electron,[11–14] and scanning probe-based[15–18] microscopies enable routine imaging with nanometer and atomic-scale resolution. However, while the in-plane image contrast from these measurements is usually related to height variations, it is oftentimes challenging to obtain the quantitative height maps from these results, especially at the nanoscale.[2,3] Although cross-sectional imaging can directly provide surface height profiles, it requires destructive cutting that can perturb the intrinsic topography of soft samples.[19,20] Moreover, it is not compatible with in situ or dynamic processes and does not provide the full 3D surface profiles. Another method to obtain quantitative surface profile is nano-tomography, which reconstructs 3D morphologies by collecting signal from a series of different angles.[20–22] However, this approach requires a small 3D volume of the samples. As a result, it is incompatible with macroscopic

systems where the interior cannot be accessed, such as integrated circuit boards, pipeline coatings, and skin biopsies.

To nondestructively quantify surface profiles of arbitrary samples, two types of approaches have been employed, the noncontact and (pseudo-)contact methods.[4,5,23] The former is mainly based on optical imaging and interferometry, which can achieve nanometer z-resolution but is limited to the diffraction limit (micron scale) along the in-plane directions.[24,25] Contact and pseudo-contact methods include stylus profilometer, scanning tunneling microscopy (STM), and AFM, all of which require the use of a mechanical probe to scan across the sample surface. These scanning probe-based methods, especially AFM, have found widespread applications in topographic mapping of various nanostructures.[18] However, due to the finite size and tip radius of the probe, the measured surface profiles tend to be broadened.[23,26–28] Such tip-convolution effects become a serious problem when the curvature or sharpness of the surface structure is comparable to or higher than that of the probe.

In the past few decades, various efforts have been made on removing tip-convolution in AFM images to recover the intrinsic surface profiles of the sample, as can be classified into three categories. One is analytical reconstruction, where the shape of the probe is determined from the measured images, and then subtracted to obtain more accurate height profiles.[26,29–32] Despite the mathematical rigor, these analytical methods have found limited applications due to their inability to deconvolute the inevitable experimental noises and imperfections in tip-sample contact such as feedback errors, lateral force variations, and inhomogeneous electrostatic interactions.[30,33–35] Another method is localization AFM (LAFM),[28] which adopts strategies used in super-resolution optical imaging, and improves the AFM resolution by localizing and statistically averaging features of interest. While LAFM is powerful in overcoming the resolution limit of traditional AFM, it selectively enhances local features and cannot provide quantitative overall height profiles of the imaged areas; in addition, the requirement of statistical averaging of identical molecules/particles prevents its application in imaging dynamic processes. The third type of tip-deconvolution approach is machine learning or deep learning. In the past decade, DL has been used in almost all types of imaging methods,[36–40] with the goal of resolution enhancement[41–44] and/or pattern recognition.[44–46] Surprisingly, the application of DL in quantitative height profiling is rare, leaving a large gap in this important field.[44,47]

In contrast to resolution enhancement and pattern recognition problems where DL outputs are non-physical contrast/intensity values, surface profiling requires continuum outputs of physical height values, which makes DL a challenging task.[48,49] In this work, we overcome this problem by using a supervised learning methodology with an encoder-decoder based neural network and achieve precise nanoscale surface profiling by combining AFM with DL. We demonstrate the capability of our approach by profiling various virtual and experimental surface structures with a large range of morphology and roughness levels. In our protocol, once the neural network is trained with a sufficient set of elementary nanostructures, it can be directly deployed for height profiling of other types of surface morphologies. The results set the stage for precise, automatic surface profiling of a large range of materials and biological systems with multiscale heterogeneities by combining DL with mechanical probes.

To enable supervised learning, we first prepare datasets of input-output pairs of tip-convoluted and deconvoluted (ground truth) images (Figure 1a, d).[50,51] These datasets can be created either from simulation or from AFM experiments, as discussed in detail in the following sections. Once a dataset is obtained, we split it in two, one for training the model and the other for testing the trained model. For the DL process, we choose an encoder-decoder type neural network model (also known as an auto-encoder, Figure 1b), which has been shown to be powerful for image-to-image translation.[52] To retain the true height values for precise surface profiling, no preprocessing steps such as normalization or standardization[53] are applied to the training datasets.

We then pass a batch of n tip-convoluted images through the model to obtain the predictions (Figure 1c), which initially are typically random before the training process. To start the training, we first calculate the error between the output images and corresponding ground truths using a loss function E_i (Figure 1e). In this study, we choose to primarily work with mean squared error (MSE) and mean absolute error (MAE) losses. The calculated error is then passed on to an optimizer which updates the network parameters. After a finite number of iterations (or epochs), when the error plateaus to a small value, the training is stopped (Supporting Information, Figure S1). Additional details of the neural network and hyperparameters used for training are provided in Methods and Tables S1 and S3 (Supporting Information). The trained DL model is then tested using the test dataset to verify the accuracy of the height profile deconvolution process.

To obtain surface corrugation features, we begin by creating virtual ground truth topographic images with randomly distributed nanostructures, including nanodomes, nanocuboids, nanoprisms, and nanocylinders. These geometries can be viewed as the "primary shapes" from which more complex corrugation features can be built. The lateral sizes of these nanostructures are chosen from a continuous uniform distribution (from 16 to 20 nm). The variety in feature sizes and shapes facilitates efficient DL deconvolution of different surface corrugation profiles. To produce the "tip-convoluted" images of these virtual nanostructures, we define a cone-shaped probe with size and curvature close to the ones widely used in AFM experiments (Figure S2). The simulated ground truth images are then dilated using this model tip shape, to obtain virtual AFM images (Figure S3). We then use such convoluted AFM image – ground truth pairs to train our neural network model following the established protocols (as shown in Figure 1).

The trained model's performance on a series of simple surface corrugations from the test dataset is shown in Figure 2. From the comparison of images and representative cross section profiles (Figure 2a–d), we already observe an effective removal of tip convolution effects and the nearly perfect recovery of the quantitative height profiles in the DL outputs. For these isolated protrusion features, tip convolution effects are mainly manifested as the broadening of the projected in-plane surface area. Therefore, to thoroughly quantify the accuracy of the DL model, we calculate the surface area of each protrusion from the tip-convoluted, DL output, and ground truth images in the entire test dataset, and plot the histograms for each type of protrusion features (Figure 2e–g). Due to the significant tip convolution of these nanoscale corrugations, the surface area of the original virtual AFM profiles strongly deviates from the ground truth, reaching 284.3%, 434.2%, and 318.6% for the domes, cuboids, and miscellaneous shapes, respectively. In contrast, the DL output only exhibits a small deviation of 8.15%, 6.41%, and 14.85% for these three types of shapes. This

demonstrates the capability of our trained model in highly accurate spatial height profiling of simple surface nano-corrugation features.

Now that our DL model has successfully deconvoluted isolated features, we further examine its capability in profiling random, continuous surface corrugations. Many realistic rough surfaces in nature are fractal with corrugations at multiple length scales.[54] Utilizing concepts from fractal geometry, we create virtual isotropically-distributed rough surfaces with an RMS (root mean squared) roughness of 5 nm. This roughness is chosen to reflect common materials in nanoscience such as thin films[55,56] and many biological components such as cell membranes.[57,58] Detailed procedures for dataset preparation are provided in Methods. Following similar protocols and using the same tip geometry as earlier (Figure S2), we prepare convoluted AFM image – ground truth pairs, and train the neural network.

The trained network's performance on a representative test image is shown in Figure 3. While the DL output does not recover all the fine details of the ground truth image, it effectively reproduces the contour profiles for features larger than ~10 nm, with an accuracy of 2-3 nm. A few representative examples of such contours are highlighted by the black dashed lines in Figure 3d–f, where we observe mismatch between the virtual AFM image and ground truth in the scale of 5-10 nm (close to the 10 nm tip radius), in contrast to the close match between DL output and ground truth within ~2 nm. Additional examples of the test results, shown in Figures S4 and S5, reveal similar accuracy of the DL outputs. To further quantify the precision of the DL model, we calculate the average surface roughness for each of the 400 test images, and plot the histogram for all the images (Figure 3g). The ground truth images have an average roughness Ra of 4.01 ± 0.10 nm (note that Ra is different from RMS roughness by definition), which is reduced to 3.75 ± 0.17 nm in the virtual AFM images due to tip convolution effects. After DL, the roughness is recovered to 3.90 ± 0.12 nm, close to that of the ground truth. Such improvements will be important for the further quantification of various structure-function relationships of rough surfaces.[59,60]

The high accuracy of the DL model is remarkable considering the randomness of the corrugation features. Note that the ultimate precision of the DL model for the virtual datasets will be limited by the simplified image dilation process used to produce virtual AFM images (Figure S3), which leads to complete removal of small concave features. In realistic experiments, while such features may not be directly accessible to the AFM probe, it can still affect the image through long-range tip-sample interactions. Therefore, although the training process will likely be more complicated for experimental images, the ultimate accuracy of a fully developed, well-trained DL model is expected to be higher for experimental results than the simplified virtual images shown above.

So far we have only considered dilation effects as a source of AFM image convolution. Realistic AFM images are typically more complicated with the presence of various other artifacts, such as line-like artifacts and edge elevation.[61,62] To examine the effectiveness of our DL model in deconvoluting these extra convolutions, we have further created virtual AFM images with the additional artifacts included and tested the DL model. As shown in Figures S6–S8, we find that the DL remains highly successful in precise surface profiling even in the co-existence of multiple types of artifacts.

We now move on to test the effectiveness of our DL model on experimental data. For this purpose, ideal experimental samples should both represent the heterogeneous morphology and composition that are typical in realistic systems, and are simple enough to enable benchmarking of the DL model. We choose submonolayer, ligand-covered nanoparticles coated on flat silicon substrates, which fulfil both requirements. We synthesize two sets of nanoparticles, Au nanospheres and Pd nanoparticles with miscellaneous shapes (cuboids, triangular prisms, etc.). From the transmission electron microscopy (TEM) images (Figure 4a, b), we confirm the nearly perfect spherical shape of the Au nanospheres, and the irregular surface morphology of Pd nanoparticles. Note that the loosely packed organic ligands on the Au or Pd particle surface, if present, should be invisible in the TEM images.[63–65] The small clusters observed on the Pd particle surfaces likely correspond to either dense aggregates of ligands or other contamination/impurity species.

We use a Tap150Al-G AFM probe (NanoAndMore), with a nominal tip radius of ~10 nm, to image all the nanoparticle samples via AC mode (amplitude modulation). Considering that the Au nanospheres have well-defined height profiles, we use part of these imaging data to train the DL model. Compared to the model used for the virtual datasets, the DL model layer sizes and the network depth are modified to optimize the training of experimental datasets (Tables S2 and S3). After the training is completed, we then use the DL network to produce deconvoluted height profiles of both the Au nanosphere and irregular Pd nanoparticle samples. As shown in Figure 4c–h, the DL model effectively removes the broadening effect due to tip convolution and retains the accurate maximum height. For the Au nanospheres, we further calculate the aspect ratio (ratio of in-plane diameter to height) of all the original AFM profiles and the corresponding DL outputs in the test dataset (Figure 4i). We observe an original aspect ratio of 1.82±0.23 nm, which is reduced to 0.93±0.16 nm in the DL output, consistent with the observed spherical profiles. This near-unity aspect ratio proves the successful, precise height profiling capabilities of the DL model for experimental AFM images.

In addition, we have quantified the in-plane radius of the Au nanospheres, and find it to reduce from 19.88±6.32 nm to 10.55±4.44 nm after DL (Figure 4j). In contrast, the mean radius obtained from TEM is 6.06 ± 0.67 nm (Figures S9 and 4j). Considering the weak sensitivity of TEM to organic ligands, the ~4.5 nm difference between AFM DL outputs and TEM can be attributed to the thickness of the ligand layer on the Au nanospheres. Note that this difference cannot be ascribed to possible inaccuracies of the DL model, as a ~4.5 nm broadening in in-plane radius would have induced significant distortion of the aspect ratio of the DL output profiles. Similarly, for Pd nanoparticles, we observe a decrease of the in-plane area from 1137±225 nm^2 to 241±97 nm^2 after DL in the AFM images, compared to 166±36 nm^2 in TEM (Figure 4k). We also attribute the excess area of ~75 nm^2 in AFM DL profiles to the additional ligand molecules not observed in TEM. These results demonstrate the capability of our combined AFM and DL approach to quantify morphologies that are otherwise invisible in other imaging methods.

In summary, we have developed a deep learning method which, combined with AFM imaging, enables precise nanoscale surface height profiling. We have used this method to successfully profile a large range of elementary nanoscale shapes as well as random, continuous surface corrugations. Future developments may aim at directly integrating this method to AFM

instruments to enable automatic, real-time determination of precise surface profiles during the imaging process.

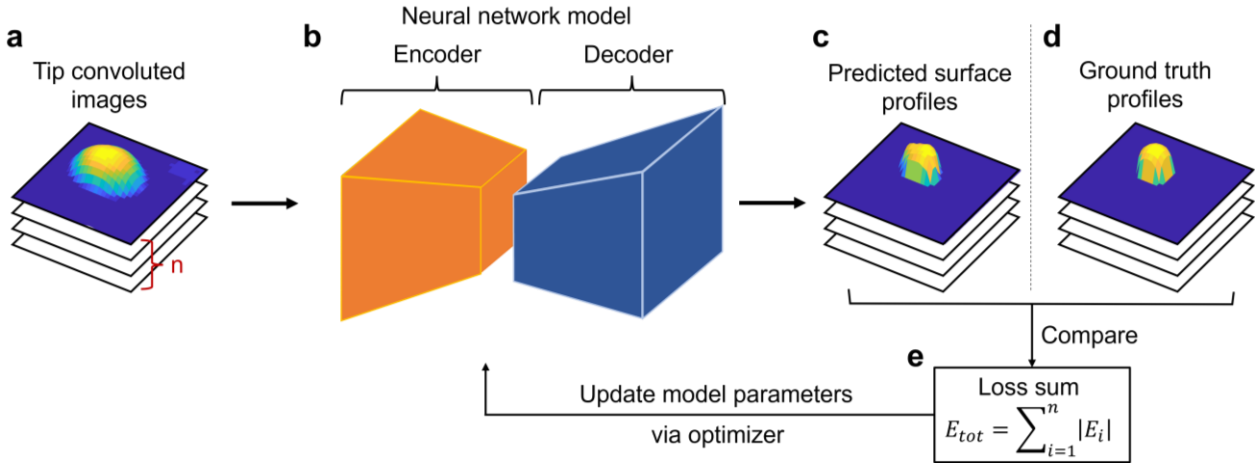

Figure 1. Schematic of our DL training process for precise surface profiling. After providing the raw AFM image as input (a), the DL model goes through reiterative training process (b–e), until the loss becomes negligible or converges to a constant small value.

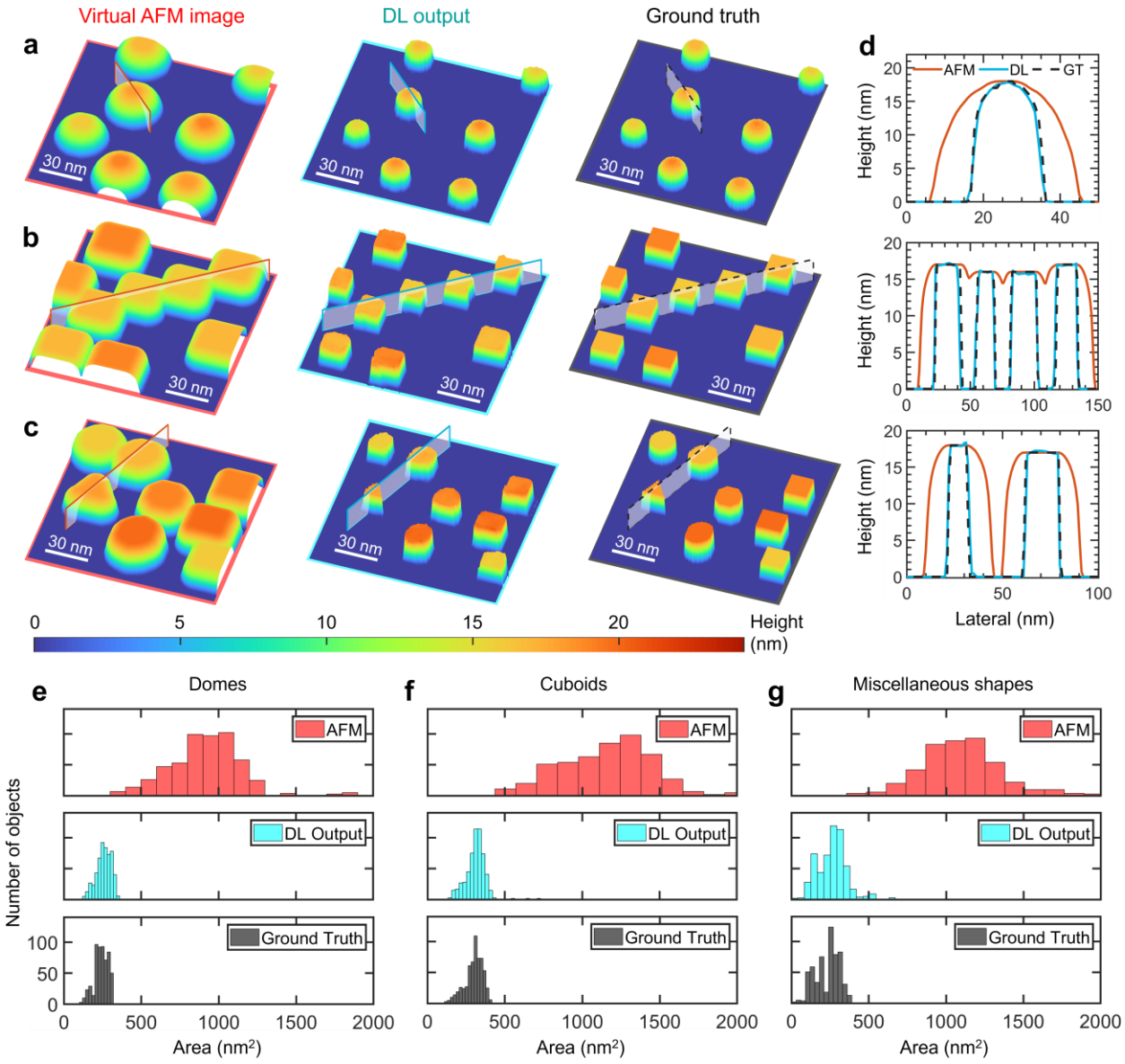

Figure 2. DL-assisted surface profiling of virtual elementary nanoscale morphologies. Virtual AFM images, DL model predictions and ground truth images of (a) nanodomes, (b) nanocuboids, and (c) miscellaneous nano-objects. (d) The cross-sectional height profiles of the corresponding images (shown on the left). GT: ground truth. (e–g) Histograms of the projected in-plane area of particles extracted from the entire test dataset.

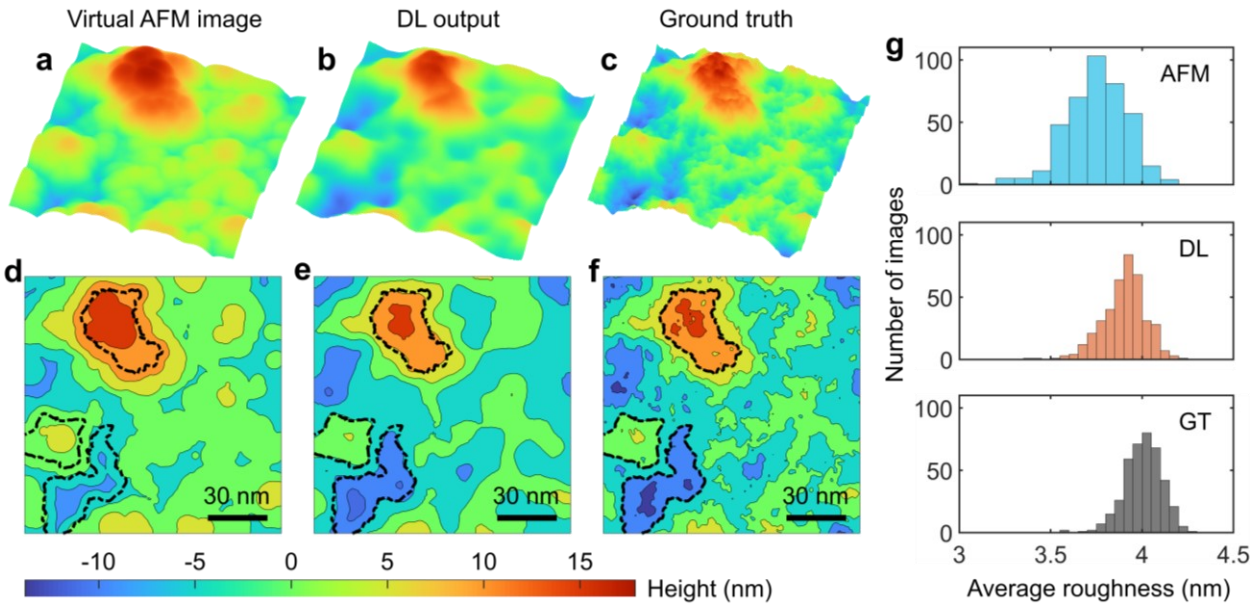

Figure 3. DL-assisted surface profiling of a random, continuous rough surface. (a) Virtual AFM image, (b) DL output, and (c) corresponding ground truth surface. (d), (e) and (f) are contour plots corresponding to (a), (b) and (c), respectively. (g) Histograms of the average roughness extracted from all the images in the test dataset.

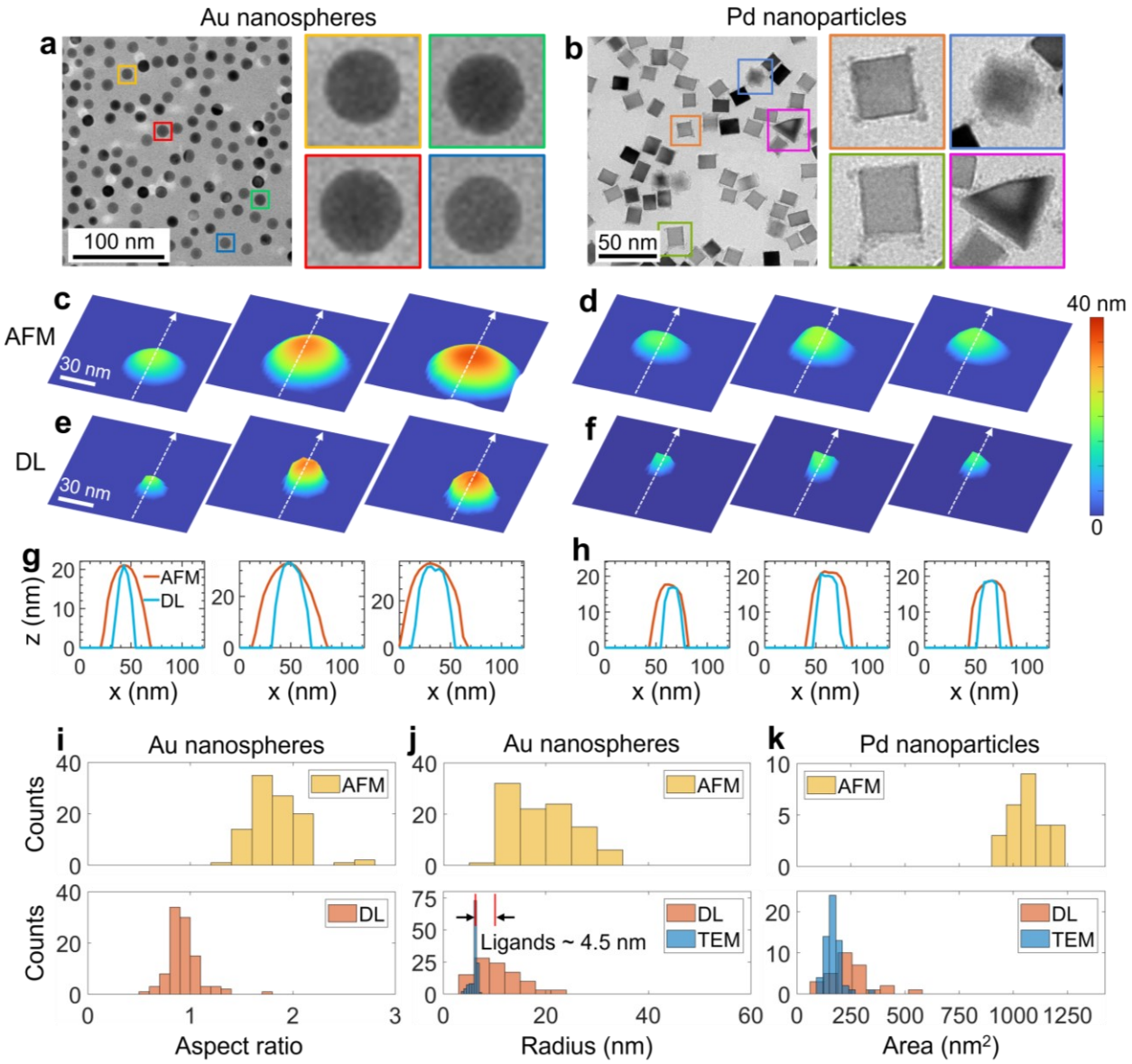

Figure 4. DL-assisted surface profiling of experimental nano-corrugations. (a) and (b) are TEM images of Au nanospheres and irregular Pd nanoparticles, respectively. The color-framed individual particle images are extracted from the large area images at locations marked by boxes of the same color. (c) and (d) are original AFM images of Au nanospheres and Pd nanoparticles coated on Si, respectively. The corresponding DL-predicted accurate profiles are shown in (e) and (f), respectively, with representative line profiles specified in (g) and (h). (i–k) are histograms extracted from original AFM images and DL outputs showing the aspect ratio (in-plane diameter vs height) of Au nanospheres (i), radius of Au nanospheres (j), and projected in-plane area of Pd nanoparticles (k). In (j) and (k) the histograms are also compared to those extracted from the corresponding TEM images.

Associated Content

Supporting Information

The supporting information is available online free of charge.

Methods: neural network preparation and training, creation of virtual AFM images, nanoparticle synthesis, nanoparticle imaging, nanoparticle size analysis from TEM, DL process using experimental AFM images. Supporting Figures S1–S9: loss vs epoch curves, schematic of the generated virtual AFM probe, schematic depicting the dilation of a surface by the virtual AFM probe, additional examples of DL-assisted height profiling of random, continuous virtual surface corrugations (3D view and contour view), DL-assisted tip deconvolution of virtual morphologies with line-like and edge-lift artifacts, TEM image analysis. Supporting Tables S1–S3: details of the encoder-decoder networks used for virtual and experimental datasets, fine-tuned hyperparameters used for training the neural network model.

Supporting Code and Data: IPython notebook for preparing virtual AFM datasets and initializing and training the neural network model (original and PDF versions) and data matrix for the generated virtual AFM probe.

Notes

The authors declare no competing financial interest.

Acknowledgements

L.K.S.B. and Y.Z. acknowledge the support from the National Science Foundation under Grant No. 2137147. Z.W., S.Z. and Y.Z. acknowledge the support from the Beckman Young Investigator Award provided by the Arnold and Mabel Beckman Foundation. The experiments were performed in part in the Carl R. Woese Institute for Genomic Biology and in the Materials Research Laboratory at the University of Illinois.

References

(1) Assender, H.; Bliznyuk, V.; Porfyrakis, K. How Surface Topography Relates to Materials' Properties. *Science* **2002**, *297* (5583), 973–976. https://doi.org/10.1126/science.1074955.

(2) Orji, N. G.; Badaroglu, M.; Barnes, B. M.; Beitia, C.; Bunday, B. D.; Celano, U.; Kline, R. J.; Neisser, M.; Obeng, Y.; Vladar, A. E. Metrology for the next Generation of Semiconductor Devices. *Nat. Electron.* **2018**, *1* (10), 532–547. https://doi.org/10.1038/s41928-018-0150-9.

(3) Vogel, E. Technology and Metrology of New Electronic Materials and Devices. *Nat. Nanotechnol.* **2007**, *2* (1), 25–32. https://doi.org/10.1038/nnano.2006.142.

(4) Adamson, A. W.; Gast, A. P. *Physical Chemistry of Surfaces*, 6th ed.; Wiley: New York, 1997.

(5) Israelachvili, J. N. *Intermolecular and Surface Forces*, 3rd ed.; Academic Press: Burlington, MA, 2011.

(6) Tudureanu, R.; Handrea-Dragan, I. M.; Boca, S.; Botiz, I. Insight and Recent Advances into the Role of Topography on the Cell Differentiation and Proliferation on Biopolymeric Surfaces. *Int. J. Mol. Sci.* **2022**, *23* (14), 7731. https://doi.org/10.3390/ijms23147731.

(7) Huang, B.; Bates, M.; Zhuang, X. Super-Resolution Fluorescence Microscopy. *Annu. Rev. Biochem.* **2009**, *78* (1), 993–1016. https://doi.org/10.1146/annurev.biochem.77.061906.092014.
(8) Chen, B.-C.; Legant, W. R.; Wang, K.; Shao, L.; Milkie, D. E.; Davidson, M. W.; Janetopoulos, C.; Wu, X. S.; Hammer, J. A.; Liu, Z.; English, B. P.; Mimori-Kiyosue, Y.; Romero, D. P.; Ritter, A. T.; Lippincott-Schwartz, J.; Fritz-Laylin, L.; Mullins, R. D.; Mitchell, D. M.; Bembenek, J. N.; Reymann, A.-C.; Böhme, R.; Grill, S. W.; Wang, J. T.; Seydoux, G.; Tulu, U. S.; Kiehart, D. P.; Betzig, E. Lattice Light-Sheet Microscopy: Imaging Molecules to Embryos at High Spatiotemporal Resolution. *Science* **2014**, *346* (6208), 1257998. https://doi.org/10.1126/science.1257998.
(9) Zhang, R.; Zhang, Y.; Dong, Z. C.; Jiang, S.; Zhang, C.; Chen, L. G.; Zhang, L.; Liao, Y.; Aizpurua, J.; Luo, Y.; Yang, J. L.; Hou, J. G. Chemical Mapping of a Single Molecule by Plasmon-Enhanced Raman Scattering. *Nature* **2013**, *498* (7452), 82–86. https://doi.org/10.1038/nature12151.
(10) Li, J. F.; Huang, Y. F.; Ding, Y.; Yang, Z. L.; Li, S. B.; Zhou, X. S.; Fan, F. R.; Zhang, W.; Zhou, Z. Y.; Wu, D. Y.; Ren, B.; Wang, Z. L.; Tian, Z. Q. Shell-Isolated Nanoparticle-Enhanced Raman Spectroscopy. *Nature* **2010**, *464* (7287), 392–395. https://doi.org/10.1038/nature08907.
(11) Wrapp, D.; Wang, N.; Corbett, K. S.; Goldsmith, J. A.; Hsieh, C.-L.; Abiona, O.; Graham, B. S.; McLellan, J. S. Cryo-EM Structure of the 2019-nCoV Spike in the Prefusion Conformation. *Science* **2020**, *367* (6483), 1260–1263. https://doi.org/10.1126/science.abb2507.
(12) Zuo, J. M.; Spence, J. C. H. *Advanced Transmission Electron Microscopy: Imaging and Diffraction in Nanoscience*; Springer: New York, 2017. https://doi.org/10.1007/978-1-4939-6607-3.
(13) Zewail, A. H. Four-Dimensional Electron Microscopy. *Science* **2010**, *328* (5975), 187–193. https://doi.org/10.1126/science.1166135.
(14) Miao, J.; Ercius, P.; Billinge, S. J. L. Atomic Electron Tomography: 3D Structures without Crystals. *Science* **2016**, *353* (6306), aaf2157–aaf2157. https://doi.org/10.1126/science.aaf2157.
(15) Ando, T.; Kodera, N.; Takai, E.; Maruyama, D.; Saito, K.; Toda, A. A High-Speed Atomic Force Microscope for Studying Biological Macromolecules. *Proc. Natl. Acad. Sci.* **2001**, *98* (22), 12468–12472. https://doi.org/10.1073/pnas.211400898.
(16) Gross, L.; Mohn, F.; Moll, N.; Liljeroth, P.; Meyer, G. The Chemical Structure of a Molecule Resolved by Atomic Force Microscopy. *Science* **2009**, *325* (5944), 1110–1114. https://doi.org/10.1126/science.1176210.
(17) Zhang, J.; Chen, P.; Yuan, B.; Ji, W.; Cheng, Z.; Qiu, X. Real-Space Identification of Intermolecular Bonding with Atomic Force Microscopy. *Science* **2013**, *342* (6158), 611–614. https://doi.org/10.1126/science.1242603.
(18) García, R. Dynamic Atomic Force Microscopy Methods. *Surf. Sci. Rep.* **2002**, *47* (6–8), 197–301. https://doi.org/10.1016/S0167-5729(02)00077-8.
(19) Midgley, P. A.; Ward, E. P. W.; Hungría, A. B.; Thomas, J. M. Nanotomography in the Chemical, Biological and Materials Sciences. *Chem. Soc. Rev.* **2007**, *36* (9), 1477. https://doi.org/10.1039/b701569k.
(20) *Electron Tomography: Methods for Three-Dimensional Visualization of Structures in the Cell*, 2nd ed.; Frank, J., Ed.; Springer: New York ; London, 2006.

(21) Atre, A. C.; Brenny, B. J. M.; Coenen, T.; García-Etxarri, A.; Polman, A.; Dionne, J. A. Nanoscale Optical Tomography with Cathodoluminescence Spectroscopy. *Nat. Nanotechnol.* **2015**, *10* (5), 429–436. https://doi.org/10.1038/nnano.2015.39.
(22) Jiang, X.; Seidler, M.; Butterfoss, G. L.; Luo, X.; Yu, T.; Xuan, S.; Prendergast, D.; Zuckermann, R. N.; Balsara, N. P. Atomic-Scale Corrugations in Crystalline Polypeptoid Nanosheets Revealed by Three-Dimensional Cryogenic Electron Microscopy. *ACS Macro Lett.* **2023**, *12* (5), 632–638. https://doi.org/10.1021/acsmacrolett.3c00101.
(23) Oura, K.; Katayama, M.; Zotov, A. V.; Lifshits, V. G.; Saranin, A. A. Surface Analysis IV. Microscopy. In *Surface Science*; Advanced Texts in Physics; Springer Berlin Heidelberg: Berlin, Heidelberg, 2003; pp 145–169. https://doi.org/10.1007/978-3-662-05179-5_7.
(24) Lee, C.-H.; Mong, H.-Y.; Lin, W.-C. Noninterferometric Wide-Field Optical Profilometry with Nanometer Depth Resolution. *Opt. Lett.* **2002**, *27* (20), 1773. https://doi.org/10.1364/OL.27.001773.
(25) Klein, S.; Petersen, S.; Taylor, U.; Rath, D.; Barcikowski, S. Quantitative Visualization of Colloidal and Intracellular Gold Nanoparticles by Confocal Microscopy. *J. Biomed. Opt.* **2010**, *15* (3), 036015. https://doi.org/10.1117/1.3461170.
(26) Keller, D. Reconstruction of STM and AFM Images Distorted by Finite-Size Tips. *Surf. Sci.* **1991**, *253* (1–3), 353–364. https://doi.org/10.1016/0039-6028(91)90606-S.
(27) Tian, F.; Qian, X.; Villarrubia, J. S. Blind Estimation of General Tip Shape in AFM Imaging. *Ultramicroscopy* **2008**, *109* (1), 44–53. https://doi.org/10.1016/j.ultramic.2008.08.002.
(28) Heath, G. R.; Kots, E.; Robertson, J. L.; Lansky, S.; Khelashvili, G.; Weinstein, H.; Scheuring, S. Localization Atomic Force Microscopy. *Nature* **2021**, *594* (7863), 385–390. https://doi.org/10.1038/s41586-021-03551-x.
(29) Villarrubia, J. S. Morphological Estimation of Tip Geometry for Scanned Probe Microscopy. *Surf. Sci.* **1994**, *321* (3), 287–300. https://doi.org/10.1016/0039-6028(94)90194-5.
(30) Villarrubia, J. S. Algorithms for Scanned Probe Microscope Image Simulation, Surface Reconstruction, and Tip Estimation. *J. Res. Natl. Inst. Stand. Technol.* **1997**, *102* (4), 425. https://doi.org/10.6028/jres.102.030.
(31) Xu, S.; Arnsdorf, M. F. Calibration of the Scanning (Atomic) Force Microscope with Gold Particles. *J. Microsc.* **1994**, *173* (3), 199–210. https://doi.org/10.1111/j.1365-2818.1994.tb03442.x.
(32) Vesenka, J.; Miller, R.; Henderson, E. Three-Dimensional Probe Reconstruction for Atomic Force Microscopy. *Rev. Sci. Instrum.* **1994**, *65* (7), 2249–2251. https://doi.org/10.1063/1.1144735.
(33) Payam, A. F.; Ramos, J. R.; Garcia, R. Molecular and Nanoscale Compositional Contrast of Soft Matter in Liquid: Interplay between Elastic and Dissipative Interactions. *ACS Nano* **2012**, *6* (6), 4663–4670. https://doi.org/10.1021/nn2048558.
(34) Pérez, R.; Štich, I.; Payne, M. C.; Terakura, K. Surface-Tip Interactions in Noncontact Atomic-Force Microscopy on Reactive Surfaces: Si(111). *Phys. Rev. B* **1998**, *58* (16), 10835–10849. https://doi.org/10.1103/PhysRevB.58.10835.
(35) Cha, W.; Campbell, M. F.; Hasz, K.; Nicaise, S. M.; Lilley, D. E.; Sato, T.; Carpick, R. W.; Bargatin, I. Hollow Atomic Force Microscopy Cantilevers with Nanoscale Wall Thicknesses. *Small* **2021**, *17* (51), 2102979. https://doi.org/10.1002/smll.202102979.

(36) Choudhary, K.; DeCost, B.; Chen, C.; Jain, A.; Tavazza, F.; Cohn, R.; Park, C. W.; Choudhary, A.; Agrawal, A.; Billinge, S. J. L.; Holm, E.; Ong, S. P.; Wolverton, C. Recent Advances and Applications of Deep Learning Methods in Materials Science. *Npj Comput. Mater.* **2022**, *8* (1), 59. https://doi.org/10.1038/s41524-022-00734-6.
(37) Ge, M.; Su, F.; Zhao, Z.; Su, D. Deep Learning Analysis on Microscopic Imaging in Materials Science. *Mater. Today Nano* **2020**, *11*, 100087. https://doi.org/10.1016/j.mtnano.2020.100087.
(38) Kalinin, S. V.; Ziatdinov, M.; Spurgeon, S. R.; Ophus, C.; Stach, E. A.; Susi, T.; Agar, J.; Randall, J. Deep Learning for Electron and Scanning Probe Microscopy: From Materials Design to Atomic Fabrication. *MRS Bull.* **2022**, *47* (9), 931–939. https://doi.org/10.1557/s43577-022-00413-3.
(39) Nguyen, L. T. P.; Liu, B. H. Emerging Machine Learning Strategies for Diminishing Measurement Uncertainty in SPM Nanometrology. *Surf. Topogr. Metrol. Prop.* **2022**, *10* (3), 033002. https://doi.org/10.1088/2051-672X/ac8a62.
(40) Kalinin, S. V.; Strelcov, E.; Belianinov, A.; Somnath, S.; Vasudevan, R. K.; Lingerfelt, E. J.; Archibald, R. K.; Chen, C.; Proksch, R.; Laanait, N.; Jesse, S. Big, Deep, and Smart Data in Scanning Probe Microscopy. *ACS Nano* **2016**, *10* (10), 9068–9086. https://doi.org/10.1021/acsnano.6b04212.
(41) Matsunaga, Y.; Fuchigami, S.; Ogane, T.; Takada, S. End-to-End Differentiable Blind Tip Reconstruction for Noisy Atomic Force Microscopy Images. *Sci. Rep.* **2023**, *13* (1), 129. https://doi.org/10.1038/s41598-022-27057-2.
(42) Kim, Y.; Lim, J.; Kim, D. Accelerating AFM Characterization via Deep-Learning-Based Image Super-Resolution. *Small* **2022**, *18* (3), 2103779. https://doi.org/10.1002/smll.202103779.
(43) Liu, Y.; Sun, Q.; Lu, W.; Wang, H.; Sun, Y.; Wang, Z.; Lu, X.; Zeng, K. General Resolution Enhancement Method in Atomic Force Microscopy Using Deep Learning. *Adv. Theory Simul.* **2019**, *2* (2), 1800137. https://doi.org/10.1002/adts.201800137.
(44) Alldritt, B.; Hapala, P.; Oinonen, N.; Urtev, F.; Krejci, O.; Federici Canova, F.; Kannala, J.; Schulz, F.; Liljeroth, P.; Foster, A. S. Automated Structure Discovery in Atomic Force Microscopy. *Sci. Adv.* **2020**, *6* (9), eaay6913. https://doi.org/10.1126/sciadv.aay6913.
(45) Gordon, O. M.; Hodgkinson, J. E. A.; Farley, S. M.; Hunsicker, E. L.; Moriarty, P. J. Automated Searching and Identification of Self-Organized Nanostructures. *Nano Lett.* **2020**, *20* (10), 7688–7693. https://doi.org/10.1021/acs.nanolett.0c03213.
(46) Okunev, A. G.; Nartova, A. V.; Matveev, A. V. Recognition of Nanoparticles on Scanning Probe Microscopy Images Using Computer Vision and Deep Machine Learning. In *2019 International Multi-Conference on Engineering, Computer and Information Sciences (SIBIRCON)*; IEEE: Novosibirsk, Russia, 2019; pp 0940–0943. https://doi.org/10.1109/SIBIRCON48586.2019.8958363.
(47) Carracedo-Cosme, J.; Romero-Muñiz, C.; Pérez, R. A Deep Learning Approach for Molecular Classification Based on AFM Images. *Nanomaterials* **2021**, *11* (7), 1658. https://doi.org/10.3390/nano11071658.
(48) Mertan, A.; Duff, D. J.; Unal, G. Single Image Depth Estimation: An Overview. *Digit. Signal Process.* **2022**, *123*, 103441. https://doi.org/10.1016/j.dsp.2022.103441.
(49) Ranftl, R.; Lasinger, K.; Hafner, D.; Schindler, K.; Koltun, V. Towards Robust Monocular Depth Estimation: Mixing Datasets for Zero-Shot Cross-Dataset Transfer. *IEEE Trans.*

Pattern Anal. Mach. Intell. **2022**, *44* (3), 1623–1637. https://doi.org/10.1109/TPAMI.2020.3019967.
(50) Goodfellow, I.; Bengio, Y.; Courville, A. *Deep Learning*; MIT Press, 2016.
(51) Alloghani, M.; Al-Jumeily, D.; Mustafina, J.; Hussain, A.; Aljaaf, A. J. A Systematic Review on Supervised and Unsupervised Machine Learning Algorithms for Data Science. In *Supervised and Unsupervised Learning for Data Science*; Berry, M. W., Mohamed, A., Yap, B. W., Eds.; Unsupervised and Semi-Supervised Learning; Springer International Publishing: Cham, 2020; pp 3–21. https://doi.org/10.1007/978-3-030-22475-2_1.
(52) Zhu, J. Y.; Zhang, R.; Pathak, D.; Darrell, T.; Efros, A. A.; Wang, O.; Shechtman, E. Toward Multimodal Image-to-Image Translation. *Adv. Neural Inf. Process. Syst.* **2017**, *2017-December*, 466–477.
(53) Pal, K. K.; Sudeep, K. S. Preprocessing for Image Classification by Convolutional Neural Networks. In *2016 IEEE International Conference on Recent Trends in Electronics, Information & Communication Technology (RTEICT)*; IEEE: Bangalore, India, 2016; pp 1778–1781. https://doi.org/10.1109/RTEICT.2016.7808140.
(54) Nayak, P. R. Random Process Model of Rough Surfaces. *J. Lubr. Technol.* **1971**, *93* (3), 398–407. https://doi.org/10.1115/1.3451608.
(55) Webb, H. K.; Truong, V. K.; Hasan, J.; Fluke, C.; Crawford, R. J.; Ivanova, E. P. Roughness Parameters for Standard Description of Surface Nanoarchitecture. *Scanning* **2012**, *34* (4), 257–263. https://doi.org/10.1002/sca.21002.
(56) Ivanova, E. P.; Truong, V. K.; Wang, J. Y.; Berndt, C. C.; Jones, R. T.; Yusuf, I. I.; Peake, I.; Schmidt, H. W.; Fluke, C.; Barnes, D.; Crawford, R. J. Impact of Nanoscale Roughness of Titanium Thin Film Surfaces on Bacterial Retention. *Langmuir* **2010**, *26* (3), 1973–1982. https://doi.org/10.1021/la902623c.
(57) D Antonio, P.; Lasalvia, M.; Perna, G.; Capozzi, V. Scale-Independent Roughness Value of Cell Membranes Studied by Means of AFM Technique. *Biochim. Biophys. Acta BBA - Biomembr.* **2012**, *1818* (12), 3141–3148. https://doi.org/10.1016/j.bbamem.2012.08.001.
(58) Girasole, M.; Pompeo, G.; Cricenti, A.; Congiu-Castellano, A.; Andreola, F.; Serafino, A.; Frazer, B. H.; Boumis, G.; Amiconi, G. Roughness of the Plasma Membrane as an Independent Morphological Parameter to Study RBCs: A Quantitative Atomic Force Microscopy Investigation. *Biochim. Biophys. Acta BBA - Biomembr.* **2007**, *1768* (5), 1268–1276. https://doi.org/10.1016/j.bbamem.2007.01.014.
(59) Quéré, D. Wetting and Roughness. *Annu. Rev. Mater. Res.* **2008**, *38* (1), 71–99. https://doi.org/10.1146/annurev.matsci.38.060407.132434.
(60) Vrijenhoek, E. M.; Hong, S.; Elimelech, M. Influence of Membrane Surface Properties on Initial Rate of Colloidal Fouling of Reverse Osmosis and Nanofiltration Membranes. *J. Membr. Sci.* **2001**, *188* (1), 115–128. https://doi.org/10.1016/S0376-7388(01)00376-3.
(61) Gołek, F.; Mazur, P.; Ryszka, Z.; Zuber, S. AFM Image Artifacts. *Appl. Surf. Sci.* **2014**, *304*, 11–19. https://doi.org/10.1016/j.apsusc.2014.01.149.
(62) Voigtländer, B. Artifacts in AFM. In *Atomic Force Microscopy*; NanoScience and Technology; Springer International Publishing: Cham, 2019; pp 137–147. https://doi.org/10.1007/978-3-030-13654-3_8.
(63) Reetz, M. T.; Helbig, W.; Quaiser, S. A.; Stimming, U.; Breuer, N.; Vogel, R. Visualization of Surfactants on Nanostructured Palladium Clusters by a Combination of STM and High-Resolution TEM. *Science* **1995**, *267* (5196), 367–369. https://doi.org/10.1126/science.267.5196.367.

(64) Merrifield, R. C.; Wang, Z. W.; Palmer, R. E.; Lead, J. R. Synthesis and Characterization of Polyvinylpyrrolidone Coated Cerium Oxide Nanoparticles. *Environ. Sci. Technol.* **2013**, *47* (21), 12426–12433. https://doi.org/10.1021/es402541z.
(65) Baalousha, M.; Lead, J. R. Rationalizing Nanomaterial Sizes Measured by Atomic Force Microscopy, Flow Field-Flow Fractionation, and Dynamic Light Scattering: Sample Preparation, Polydispersity, and Particle Structure. *Environ. Sci. Technol.* **2012**, *46* (11), 6134–6142. https://doi.org/10.1021/es301167x.

TOC Graphic: